



Future intensity–duration–frequency curves of Edmonton under climate warming and increased convective available potential energy

Chun-Chao Kuo^{1,2} · Kai Ern Gan^{3,4} · Yang Yang² · Thian Yew Gan²

Received: 6 July 2021 / Accepted: 15 October 2021 / Published online: 30 October 2021
© The Author(s), under exclusive licence to Springer Nature B.V. 2021

Abstract

A regional climate model called WRF (Weather Research and Forecasting) was set up in a two-way, three-domain nested framework to simulate future May to August precipitation of central Alberta, Canada. WRF is forced with climate outputs from four Global Climate Models (GCMs) for the baseline period 1980–2005, and for 2041–2100 based on the Representative Concentration Pathways (RCP) 4.5 and 8.5 climate scenarios of the Intergovernmental Panel on Climate Change (IPCC). A quantile–quantile bias correction method and a regional frequency analysis were applied to acquire future grid-based IDF curves for the city of Edmonton. Future trends of air temperature and convective available potential energy (CAPE) are investigated. Future IDF curves are expected to have higher intensities because of projected higher air temperature and atmospheric water vapor, and projected increase in CAPE by 2071–2100. Our results likely mean that under the impact of climate change, the future risk of flooding in Edmonton would increase.

Keywords Annual maximum precipitation · Air temperature · Convective available potential energy (CAPE) · Regional climate model (RCM) · Global Climate Model (GCM)

1 Introduction

In recent years, Canada has experienced severe storms which resulted in severe flood damages, such as the flood events of Calgary and Toronto in 2013. They were the worst natural disasters of Alberta and Ontario, and ranked the first and the third largest natural disasters in Canada, respectively (Milrad et al. 2015; ECCC 2017). The 2013 flood damage of

✉ Thian Yew Gan
tgan@ualberta.ca

¹ River Forecast Centre, Government of British Columbia, Victoria, Canada

² Department of Civil and Environmental Engineering, University of Alberta, Edmonton, AB T6G 1H9, Canada

³ Department of Computer and Information Technology, University of Pennsylvania, Philadelphia, PA 19104, USA

⁴ Department of Civil Engineering, McMaster University, Hamilton, Ontario L8S 4L7, Canada

Calgary was estimated to exceed 5 billion dollars. In central Alberta, according to the current design standard of Edmonton, the 1995, 2004, and 2012 floods were supposed to be floods of 100- to 200-year return periods. However, they had been occurring about once every 10 years. The risk R of a design flood Q_T of return period T being exceeded at least once in a project of lifespan n years is

$$R = P(X > Q_T) = 1 - \left(1 - \frac{1}{T}\right)^n \quad (1)$$

Equation (1) shows that the risk R of a design flood of $T = 200$ years will be exceeded at least once in a project life n of 25 years is only $\sim 12\%$. R increases to $\sim 22\%$ if $T = 100$ years, and $\sim 93\%$ if $T = 10$ years, which demonstrates that the risk of flooding will increase drastically given the significant decrease in return periods of recent floods.

The above severe storm events show that current intensity–duration–frequency (IDF) curves for Edmonton are obsolete because these IDF curves do not reflect recent changes to Alberta’s climatic regime given extreme storm events have been occurring more frequently in central Alberta in recent years (www.publicsafety.gc.ca/cnt/rsrscs/cndn-dsstr-dtbs/index-eng.aspx). Furthermore, recent extreme storms are capable of overwhelming existing municipal structures of Alberta and other cities of Canada.

Recent studies suggest that the variability of global precipitation is increasing due to global warming (Pendergrass et al. 2017), which could also lead to more frequent and severe future extreme storm events (Chou et al. 2012), giving rise to higher rainfall intensities in different regions worldwide (Allan and Soden 2008; Lenderink and Van Meijgaard 2008). According to the report of CMIP5 (Phase 5 of the Coupled Model Intercomparison Project), the response to CO_2 doubling in the multi-model mean of CMIP5 daily rainfall is characterized by an increase of $1\% \text{ K}^{-1}$ at all rain rates and a shift to higher rain rates of $3.3\% \text{ K}^{-1}$ (Pendergrass and Hartmann 2014). According to CMIP6, the magnitude of extreme precipitation is generally proportional to the global warming level, with an increase of about 7% per 1°C warming (Douville et al. 2021). Higher precipitation has been observed in mid- and high latitudes of the Northern Hemisphere in recent decades (e.g., Alexander et al. 2006; Wang et al. 2013). As noted by Shi and Xu (2008), approximately 54.3% of global terrestrial regions had experienced higher annual precipitation from 1951 to 2002. From a global dataset of the second half of the twentieth century, Frich et al. (2002) found a significant increase in extreme precipitation events during wet spells and a higher number of heavy rainfall events. Regional changes in precipitation have also been detected in different parts of the world (Berg et al. 2013; Bintanja and Selten 2014; Jiang et al. 2015; Adler et al. 2017; Pendergrass et al. 2017; Tariku and Gan 2018a).

Even though global warming has resulted in more frequent occurrences of intensive precipitation (Yang et al. 2019; Douville et al. 2021), jeopardizing the safety standard of existing municipal infrastructure, IDF curves derived from historic data have been regarded as stationary, falsely assuming that the mean and variance of future precipitation will still remain unchanged. Therefore, many existing IDF curves of Canadian cities are likely not representative of projected precipitation regimes under the effect of climate change. Updating existing IDF curves to reflect possible changes in climatic regimes will reduce the vulnerability of new infrastructure to future storms by providing adequate guidance for building new resilient, sustainable drainage systems to mitigate the impact of future extreme storms, e.g., the IDF_CC tool of Western Uni. (<https://www.idf-cc-uwo.ca/about>).

The future precipitation of Canada under global warming impact simulated by global (GCMs) and regional climate models (RCM) has been assessed by Mladjic et al. (2011).

Maurer et al. (2007) developed a monthly dataset based on climate projections of 16 GCMs subjected to three emission scenarios of AR4 (IPCC 2007) statistically down-scaled to a spatial resolution of $1/8^\circ$ (about 140 km^2 per grid cell) over the conterminous USA and parts of Canada and Mexico. The annual precipitation is projected to increase significantly in the Canadian Prairies (Mailhot et al. 2012), with the largest increase in central Alberta (Shepherd and McGinn 2003). Past studies on future extreme storms in Alberta were predominantly conducted at daily and multi-day (Mailhot et al. 2010; Sillmann et al. 2013), and at hourly to sub-hourly time scales (Kuo et al. 2014, 2015; Kuo and Gan 2015). Studies predominantly use statistical downscaling methods to project future IDF curves (Simonovic et al. 2016; Schardong et al. 2020), even though empirical relationships developed from the baseline period may or may not be applicable to project future precipitation.

According to CMIP5, the precipitation of central Alberta is expected to be more extreme in 2081–2100 (Sillmann et al. 2013). For example, precipitation indices, R95p (annual total precipitation when daily precipitation is higher than the 95th percentile) and R10mm (number of days when daily precipitation is larger than 10 mm), are supposed to increase by 10–70% and 0.5–4 days in 2081–2100, respectively. From Representative Concentration Pathways (RCP) 4.5 and RCP 8.5 climate scenarios of CMIP5 statistically downscaled for the 2050s (2041–2070) and 2080s (2071–2100) by the Pacific Climate Impacts Consortium (PCIC), the annual precipitation at Fort Simpson of Alberta is projected to increase by 15–32% in 2050s and 15–40% in 2080s compared with the baseline period of 1974–2004 (Scheepers et al. 2018). By statistically down-scaled climate projections of CGCM3, Hassanzadeh et al. (2014) projected that short-duration storms (1 h and 6 h) of Saskatoon will have higher intensities. On the other hand, using climate projections of CGCM3, Mailhot et al. (2010) did not detect much projected change to the intensity of annual maximum rainfall of long durations in the Canadian Prairies by the late twenty-first century. By dynamically downscaling climate projections of four GCMs using MM5 (5th Generation Pennsylvania State U. mesoscale model), the precipitation of Alberta is projected to be more intensive (Kuo et al. 2014, 2015). In this study, WRF (Weather Research Forecasting) which has better parameterization schemes than MM5 is forced with climate outputs from four GCMs.

Global warming could increase the intensity of precipitation extremes (Allan and Soden 2008) because the water-holding capacity of the atmosphere will increase at about 7% per degree Celsius in temperature (Clausius-Clapeyron scaling). Convective available potential energy (CAPE in Joules/kg), the vertical integral of parcel buoyancy between free convection and neutral buoyancy, has been widely applied to detect the occurrence of severe convective storms (Ye et al. 1998; Seeley and Romps 2015; Dong et al. 2018). For example, similar increasing and decreasing trends between CAPE and extreme precipitation indices were found for the USA and southern Canada (Gizaw et al. 2021). Murugavel et al. (2012) found that higher CAPE in India may compensate the decreased rainfall due to weakening circulation monsoon. Using downscaled climate output, we will investigate how climate warming and higher CAPE will affect the extreme precipitation and IDF curves of Alberta.

This study has three key objectives:

- (1) Investigate possible changes of annual maximum sub-daily precipitation of central Alberta based on dynamically downscaled RCP 4.5 and RCP8.5 climate scenarios by a RCM.

- (2) Investigate projected changes and trends of 2-m air temperature and CAPE, and the differences between the reference (1984–2015) and projected (2041–2100) IDF curves of Edmonton.
- (3) Derive and compare IDF curves of central Alberta developed from RCP climate scenarios of CMIP5 downscaled using the newer RCM, WRF with those previously projected using MM5, and SRES (Special Report on Emissions Scenarios) scenarios of CMIP3.

2 Data

2.1 Rain gauge data

The city of Edmonton in central Alberta, of about 700 km² in area and a rain gauge network, currently has 11 rain gauges recording data over May to August (MJJA) between 1984 and 2015 (stars in Fig. 2). The old rain gauge in the municipal airport has recorded data since 1914 but discontinued after 1995, which (circle in Fig. 2) was used to develop past IDF curves for Edmonton. Only the MJJA data used for analysis were checked for quality control, such as removing unrealistic large “individual spikes” when there was no storm recorded in nearby rain gauges. Only few stations have missing records, and the data of those years are not included in the frequency analysis. Typically, the annual maximum series is used to establish the IDF curves. However, as MJJA is the major rainy season of central Alberta with a seasonal average of 219.5 mm, data from MJJA have been widely utilized in Edmonton. In addition, most MJJA storms in central Alberta have storm durations 4 h or shorter (Kuo et al. 2015).

2.2 Climate model data

GCMs are designed to simulate global-scale climate processes at resolutions not adequate to simulate detailed, local-scale precipitation-producing weather systems, e.g., resolutions of the four GCMs selected in this study range from $0.9^\circ \times 1.3^\circ$ to $2.8^\circ \times 2.8^\circ$ (Weisman et al. 1997). Because of coarse resolutions, precipitation simulated by GCMs tends to underestimate the extreme storm events and is not ideal for developing IDF curves. A regional climate model (RCM) driven with boundary conditions simulated by GCMs can simulate local-scale climate processes subjected to global-scale processes and climate projections of GCMs forced with anthropogenic greenhouse gases. By taking advantage of both RCMs and GCMs, we could model local-scale precipitation-producing weather systems under the potential impact of climate change. From climate projections of GCMs dynamically downscaled by RCMs and corrected for biases, we could project possible changes to precipitation at temporal and spatial resolutions adequate for developing IDF curves to design municipal structures.

The RCM called WRF was used to dynamically downscale 6-hourly projected climate data of four GCMs, CanESM2 (the second-generation Canadian Earth System Model), ACCESS1-3 (versions 1–3 of Australian Community Climate and Earth-System Simulator), CCSM4 (version 4 of the Community Climate Systems Model of USA), and MIROC5 (version 5 of the Japanese GCM, Model for Interdisciplinary Research on Climate) of CMIP5 (Flato et al. 2013), selected for this study. These four GCMs are chosen partly because their earlier versions, ACCESS (Australia), CGCM3 (Canada), CCSM3 (USA),

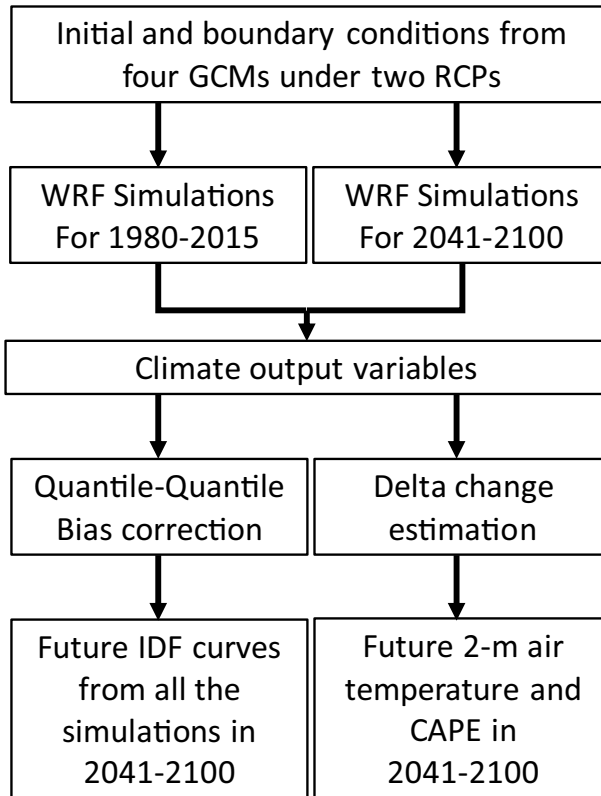


Fig. 1 Flow chart of this study using WRF to downscale two RCP climate scenarios of four GCMs to develop future IDF curves, air temperature, and CAPE of Edmonton in 2041–2100

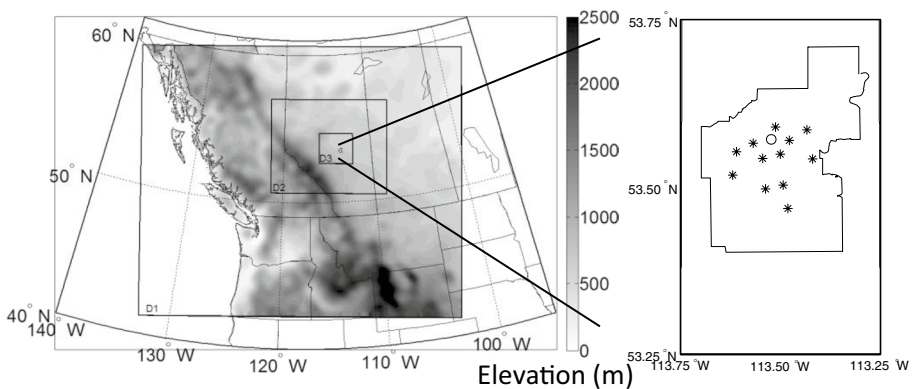


Fig. 2 WRF domain outlines (encompassed by the thin black lines) and Edmonton area with its 12 rain gauges (circle, municipal airport rain gauge; star, new rain gauges) locations

and MICOR3.2 (Japan), were chosen by Kuo et al. (2014) in a study on IDF curves of Alberta under the impact of climate change. The climate data needed to specify initial and lateral boundary conditions of WRF consist of geopotential height, air temperature, specific humidity, surface pressure, wind fields, mean sea level pressure, and sea surface temperature. The climate data of all four GCMs selected include the historical period of 1980–2005 and RCP 4.5 and 8.5 climate scenarios of 2041–2100. WRF, originally developed by NCAR or National Center for Atmospheric Research (Skamarock et al. 2008), was used to downscale eight sets of RCP climate scenarios for central Alberta in a 3-domain framework. The precipitation output of the 3rd domain of WRF at 3-km resolution was used to estimate intensities of short-duration storms for both historical and future period.

3 Research methodology

3.1 RCM configurations and post-processing

A flowchart of this study is shown in Fig. 1. WRF was first run from 1979 to 2005 using outputs of four GCMs (see Sect. 3.2) as initial and lateral boundary conditions in a two-way nesting, 3-domain configuration, with the outermost domain (D1) at 27-km resolution. The simulations of the first year (1979) were treated as spin-up. The output of D1 was used to run the second domain (D2) at 9-km resolution, and output of D2 was used to run the 3-km resolution, innermost domain (D3). A two-way nesting modeling structure means that the inner domains (D3 and D2) provide the feedback to their outer domains (D2 and D1), respectively. The purpose of the 3-domain nesting is to set up the inner most domain with a spatial resolution adequate to simulate convective storms which could be missed at resolutions coarser than 10 km. Using the Global Environmental Multiscale (GEM) model from Environment Canada, Erfani et al. (2003) concluded that a 4-km resolution model domain was adequate to simulate the climate system initiated along the Rocky Mountain foothills. Thus, the 3-km spatial resolution for D3 should be sufficient to model the small-scale convective precipitation events in Alberta. The three domains run with 40 vertical levels are shown in Fig. 2.

Unlike downscaling of SRES scenarios by running MM5 in a stand-alone mode, the land–atmosphere interaction and feedback is accounted for by coupling WRF with an LSM (land surface model) called Noah. Not accounting for this feedback may induce simulation errors in heat and water fluxes that affect the temperature and precipitation. Kanamitsu and Mo (2003) showed that soil moisture, vegetation, and land surface temperature influence latent and sensible heat fluxes, which in turn affect the air temperature and precipitation of North America. Soil moisture and temperature modulate both thermal and dynamical characteristics of land and lower atmosphere. Air temperature can vary by a few degrees Celsius by variations in land surface fluxes. Zhang et al. (2008) found strong coupling between soil moisture and daily mean temperature in the Great Plains. Mahmood et al. (2012) found that near surface soil moisture is associated with precipitation and maximum temperature, which demonstrate land-surface-atmosphere interactions. Furthermore, incorporating the land–atmosphere feedback can enhance the predictability of an RCM simulating convective storms (Ryu et al. 2016).

Key parameterizations of WRF are grouped into short wave (SW), longwave (LW), microphysics (MP), and cumulus parameterization (CP); planetary boundary layer (PBL); and land surface model (LSM). MP interacts with other climate dynamics,

radiation, aerosols/chemistry, etc., which are important components in climate modeling. CP schemes are designed for simulating sub-grid scale effects of convective and shallow clouds. In fine-tuning WRF, to simulate the regional climate of central Alberta, various physical schemes are considered by testing different combinations of climatic inputs and parameterization schemes to simulate representative climate of Alberta during wet, normal, and dry years, such as CP schemes, MP, radiation schemes, PBL, and LSM (Kerkhoven et al. 2006; Steeneveld et al. 2010; Tariku and Gan 2018b). Through results estimated from conducting various test runs, the schemes of WRF chosen are the Kain-Fritsch cumulus scheme (Kain 2004), WRF Double-Moment 6-class Microphysics scheme (Lim and Hong 2010), CAM Longwave (LW) and Shortwave (SW) radiation scheme (Collins et al. 2004), the Yonsei University PBL (planetary boundary layer) scheme (Hong et al. 2006), and the Noah LSM (Chen et al. 1996, 1997). These configurations simulated representative climate for the Mackenzie River Basin (Kuo and Gan 2018). Given developing IDF curves require sub-hourly precipitation data, the outputs of WRF at 15-min time intervals for the innermost domain (D3) were used to estimate the grid-based IDF curves of Edmonton. The D3 domain uses 30 s as the simulation time step, which means that the 15-min precipitation simulated is aggregated from the precipitation simulated at the 30-s time step. These settings were used in WRF for simulating both the climate of the baseline period 1980–2005, and the climate projections of 2041–2100 using GCM outputs.

Future projections of air temperature and CAPE within the Domain 3 (D3) were also analyzed, but data that are within 30 km to the boundary of D3 were not used to minimize the impact of boundary effects on climate variables. The downscaled 2-m air temperatures in D3 were averaged spatially and temporally for the MJJA season. Next, the MJJA air temperature anomaly for 2041–2100 was estimated by subtracting WRF's simulations with the simulated average MJJA air temperature of 1980–2005 (projected temperature – temperature of the baseline period). The projected change in CAPE in 2041–2100 was estimated by the difference in CAPE between 2041 and 2100 and the baseline average CAPE average simulated by WRF divided by the baseline average CAPE ((Projected CAPE – CAPE of baseline period)/(CAPE of baseline period) × 100%). All trend analyses were based on the Mann–Kendall trend test (Mann 1945; Kendall 1948) at a 0.05 significance level, and the trend magnitude was estimated using the Theil–Sen slope (Eq. 1) (Sen 1968; Theil 1992).

$$\beta = \text{median} \left[\frac{X_j - X_i}{j - i} \right], i, j \in \{1, n\} \quad (2)$$

where $X = \{x_1, \dots, x_i, \dots, x_n\}$, n is the length of X , and $i < j$. β is the estimated trend magnitude of X .

3.2 Intensity–duration–frequency (IDF) curves and bias correction

To develop IDF curves, we need to conduct frequency analysis for selected storm durations, which in this study are 5 min, 10 min, 15 min, 30 min, 1 h, 2 h, 6 h, 12 h, and 24 h. For each storm duration, we estimated the annual maximum rainfall intensity time series and fitted it with a generalized extreme value (GEV) distribution, which has been found suitable for modeling rainfall intensity of Canada (e.g., Mailhot et al. 2010; Hasanzadeh et al. 2014).

The cumulated density function $F(x)$ of the GEV distribution (Jenkinson 1955) is:

$$F(x) = \exp\{-[1 - k(\frac{x - \mu}{\alpha})]^{1/k}\} \tag{3}$$

where x is the rainfall intensity, and μ , α , and k are the location, scale, and shape parameters of GEV, respectively. Using the probability weighted moment (PWM) method, k is derived as:

$$\hat{k} = 7.8590C + 2.9554C^2 \tag{4}$$

where $C = \frac{2b_1 - b_0}{3b_2 - b_0} - \frac{\log 2}{\log 3}$ and b_r (r is from 0 to 2) is

$$b_r = \hat{\beta}_r = \frac{1}{N} \sum_{i=1}^N \binom{i-1}{r} x_i / \binom{N-1}{r} \tag{5}$$

x_i is the i th ranked rainfall intensity from the minimum to maximum.

After deriving \hat{k} , $\hat{\alpha}$ can be estimated using \hat{k} , b_0 , b_1 , and the Gama function (Γ):

$$\hat{\alpha} = \frac{(2b_1 - b_0)\hat{k}}{\Gamma(1 + \hat{k})(1 - 2^{-\hat{k}})} \tag{6}$$

$\hat{\mu}$ can be estimated using \hat{k} , b_0 , $\hat{\alpha}$, and the Gama function (Γ):

$$\hat{\mu} = b_0 + \frac{\hat{\alpha}}{\hat{k}} \left[\Gamma(1 + \hat{k}) - 1 \right] \tag{7}$$

Once we have derived all three parameters, the quantile estimate of a given storm duration of return period T (Jenkinson 1955) is given as:

$$\hat{x}_T = \hat{\mu} + \frac{\hat{\alpha}}{\hat{k}} \left[1 - \left\{ -\ln\left(1 - \frac{1}{T}\right) \right\}^{\hat{k}} \right] \tag{8}$$

Using the rainfall intensities of storm duration t (hours) and return period T , the IDF curve can be expressed as:

$$I = a(t + c)^b \tag{9}$$

where I is the rainfall intensity (mm/hour); a , b , and c are the parameters.

We selected 2-, 5-, 10-, 25-, 50-, and 100-year return periods in our study. IDF curves for the reference period (1984–2015) were estimated from the annual maximum precipitation of different storm durations derived from the raw 5-min precipitation data in Edmonton. Based on results from the heterogeneity test (Hosking and Wallis 1997) applied to these 11 rain gauges, this region can be regarded as spatially homogeneous. Furthermore, from the Mann–Kendall test applied at the 0.05 significance level, the test failed to reject the null hypothesis for all the 1984–2015 precipitation time series. In other words, statistically, there is insufficient evidence to consider all the 1984–2015 precipitation time series as stationary.

The past IDF curves (1914–1995) developed by the city of Edmonton were based on the EVI-MOM method (quantiles were derived from the extreme value type I probability distribution with parameters derived using the method of moment), and observations were collected from the municipal airport (shown as blue dash lines in Fig. 4). The reference IDF

curves (1984–2015) were estimated from 11 stations of rainfall data collected within the city of Edmonton using the GEV-PWM method (quantiles were derived from the General Extreme Value probability distribution with parameters derived using the probability weighted moment). As expected, results obtained from the Kolmogorov–Smirnov (K-S) test and the standard error show that the GEV-PWM distribution fits the annual maximum rainfall intensity data of these 11 gauges better than the EVI-MOM distribution, as was also shown in Kuo et al. (2013). With each grid of WRF regarded as a single site, IDF curves are estimated for individual grids located in the innermost domain (D3) using GEV-PWM instead of the EVI-MOM approach adopted in most Canadian municipalities, since the former is found to yield more accurate precipitation intensity quantiles.

We established IDF curves from precipitation simulated by WRF for storm durations ranging between 15 min, 30 min, 1 h, 2 h, 6 h, 12 h, and 24 h, and for return periods of 2 years, 5 years, 10 years, 25 years, 50 years, and 100 years. The annual maximum rainfall intensity was estimated by the moving window method for the MJJA season only, referred to as AMI-MJJA. The AMI-MJJA for storm durations other than 15 min was achieved by the moving window method applied to the AMI-MJJA data at 15-min intervals. The AMI-MJJA of each storm duration was fitted using a stationary GEV probability distribution function with parameters estimated from the PWM method (Kuo et al. 2013, 2014). On the basis of results obtained from the Kolmogorov–Smirnov (K-S) test and the standard error, the GEV-PWM distribution is adequate to model the annual maximum rainfall intensity data. Based on the probability distribution functions computed for the storm durations, multi-site IDF curves were developed. IDF curves of Figs. 4 and 5 were computed from rain gauge data (Fig. 2) and precipitation simulated by WRF for the base and future periods, which include past (1914–1995) (blue dash line) and current (1984–2015) IDF curves (gray shaded area), and WRF projected (red and magenta lines) IDF curves. The upper and lower bounds of future IDF curves based on 8 sets of future climates for central Alberta projected by four GCMs for two RCP scenarios dynamically downscaled by WRF were estimated.

Because storms simulated by WRF tend to suffer from over-estimation (positive bias), a quantile–quantile bias correction (Boé et al. 2007; Johnson and Sharma 2011; Sun et al. 2011; Xu and Yang 2012) method was employed to WRF’s simulations before the data are used to estimate IDF curves. In this method, deviates of certain probability of occurrence p obtained from the cumulative distribution function (CDF) of climate data simulated by WRF are replaced with deviates of the same probability of occurrence p obtained from the CDF of the reference period. Similar to other bias correction methods, the quantile–quantile bias correction method assumes the statistical relationship between the observed and the projected rainfall is stationary for the same climate model over different simulation periods and climate scenarios. However, given the baseline period is expected to contain a smaller range of extreme climate, applying a bias correction method for the projection periods could increase the uncertainty associated with climate projections. In this approach, a “quantile map” for both simulated and observed precipitation of the same period was created by applying an unbiased quantile estimator (Lafon et al. 2013) to the ranked data, i.e., an X value simulated by WRF was assigned a cumulative probability, p , of the CDF of WRF’s simulated rainfall intensity series (Figure S1). Next, from the CDF of observed precipitation, X' , with the same p , was the bias corrected X value (Eq. 10).

$$X' = F_{obs}^{-1}[F_{Sim}(X)] \quad (10)$$

where F_{obs}^{-1} is the (inverse) of the observed CDF and F_{Sim} is the simulated CDF.

Using the regional frequency analysis (RFA) framework of Hosking and Wallis (1997), we estimated the regional quantile curve based on the observed data and data simulated by a GCM downscaled by WRF to obtain the quantile–quantile relationship between the observed and the simulated data for the base period. Assuming spatially homogeneous conditions, this regional quantile–quantile relationship, that should be similar between the sites, was used to correct the bias of each GCM’s simulations without affecting the climate change-induced signals between the base and future periods. Each grid will have one set of IDF curves corresponding to each GCM’s downscaled simulations for each RCP scenario for 2050s and 2080s. The upper and lower bounds of projected IDF curves represent the maximum and minimum IDF curves developed respectively for a given return period in 2050s and 2080s. Lower biases are found for IDF curves derived from WRF’s simulations forced by outputs of CanESM2 (Canada) and CCSM4 (USA), and higher for those derived from WRF forced by outputs of ACCESS1-3 (Australia) and MIROC5 (Japan).

4 Results and discussion

4.1 Future projections of 2-m air temperature and CAPE

The atmospheric and surface energy budget plays a critical role in the hydrological cycle. Global warming will likely increase the severity and frequency of hydrologic extremes because warming leads to higher water-holding capacity of air (Clausius-Clapeyron relationship). The Fifth Assessment Report (AR5) of IPCC (2013) and AR6 of IPCC (2021) (Douville et al. 2021) concluded that more regions have experienced increased heavy precipitation (above the 95th percentile) events since 1951. However, the sensitivity of precipitation extremes to increased temperature varies from region to region, and it tends to be more sensitive in tropical than other regions (O’Gorman 2015). In addition, different types of precipitation extremes, such as orographic and convective storms, respond to warming differently. Two modes of change, a shift and an increase, are applied to simulations of global warming with climate models from CMIP5. As explained earlier, the response to CO₂ doubling in the multi-model mean of CMIP5 daily rainfall is characterized by an increase of 1% K⁻¹ at all rain rates and a shift to higher rain rates of 3.3% K⁻¹.

The radiative forcing of the rising concentration of greenhouse gases such as CO₂, CH₄, and N₂O leads to higher air temperature (IPCC 2007), which in turn increase the convective available potential energy (CAPE), and large CAPE has been widely used to represent conditions favorable for the occurrence of severe convective storms. Therefore, we will also discuss the projections of air temperature and CAPE based on the spatially averaged, 2-m annual air temperature anomaly at D3 for MJJA simulated by WRF over the future (2041–2100) with respect to the baseline periods (1980–2005) (Fig. 3a). Shaded blue and red plots represent the range of temperature projected by WRF driven by RCP 4.5 and RCP 8.5 climate scenarios simulated by 4 GCMs of CMIP5 for 2041–2100, respectively. As expected, the time series of temperature anomaly simulated for 2041–2100 shows consistent increasing (positive) trends, implying that central Alberta is expected to become increasingly warmer over the twenty-first century. The projected rates of increase ranging between 0.019 and 0.088 °C/year in 2041–2100 are based on rates estimated from RCP 4.5 and 8.5 scenarios of four GCMs using the Theil-Sen estimator (see Figure S2). By 2050s (2080s), the projected change in air temperature ranges from –0.4 to 6.7 °C (–1.4 °C and 10.4 °C) with an average increase of about 2.9 °C (4.3 °C). Both RCP 4.5 and RCP 8.5

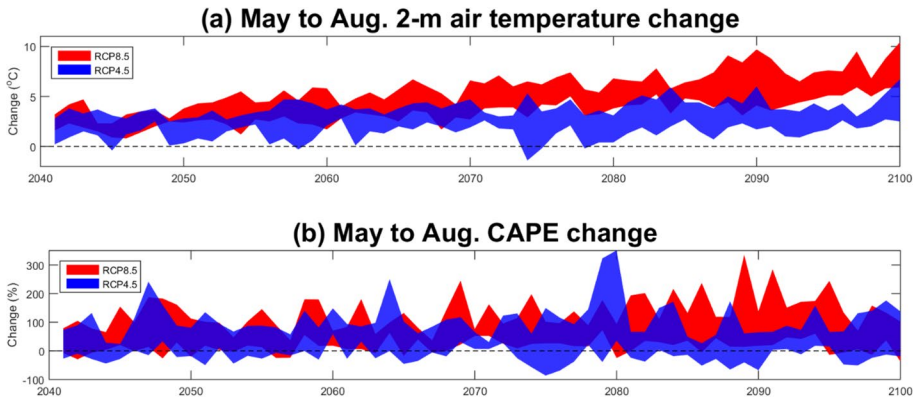


Fig. 3 **a** The annual anomaly time series of simulated D3's (Domain 3) May to Aug. 2-m temperature (temperature in the future – temperature in baseline period) (°C) projected by WRF driven by 4 GCMs under RCP 8.5 and 4.5 scenarios. **b** The annual anomaly time series of simulated D3's (Domain 3) May to Aug. CAPE (%) ((CAPE in the future – CAPE in basis period)/(CAPE in basis period) × 100%) projected by WRF driven by 4 GCMs under RCP8.5 and 4.5 scenarios

scenarios project a similar range of temperature increase in central Alberta before 2050 (Fig. 3). However, after the 2050s, RCP 8.5 scenarios projected a larger increase in air temperature, while RCP 4.5 scenarios only project a modest increase. Overall, as expected, based on the Mann–Kendall test, all these eight anomaly time series of the spatially averaged 2-m air temperature exhibit significant increasing trends at a 0.05 significance level in 2041–2100.

The spatially averaged CAPE annual anomaly at D3 for the MJJA season simulated by WRF for RCP 4.5 and RCP 8.5 scenarios also generally displays similar upward trends as the projected 2-m air temperature. In Fig. 3b, the shaded colors represent the range of projected CAPE change expressed in percentage for both dynamically downscaled RCP scenarios based on simulations of four GCMs as initial and boundary conditions. The projected increase in CAPE ranges from 0.025 to 1.40%/year in 2041–2100. The simulated time series of CAPE and trends are shown in Figure S3. The projected change in CAPE ranges from about –50 to 250% with a mean of 48.7% in 2050s, and about –86.5 to 350.8% with a mean of 60.6% in 2080s. Under the projected warming trend, the summer CAPE of central Alberta is expected to increase in 2041–2100.

Both RCP scenarios, RCP 4.5 and RCP 8.5, project a similar range of increase in CAPE in central Alberta in the 2050s and 2080s. However, in 2080–2095, a higher increase in CAPE is projected under the RCP 8.5 scenario. Based on the Mann–Kendall's test at a 0.05 significance level, three out of eight positive trends of the spatially averaged CAPE simulated in 2041–2100 are statistically significant. Although the spatially averaged CAPE simulated show an overall initial increase in 2041–2100, five out of eight cases do not continue to show an increasing trend over the period.

Projecting regional changes in precipitation patterns involves multiple uncertainties, such as uncertainties of climate models (model resolutions, parameterizations, and poorly constrained processes), climate variability, climate change scenarios, and input data. Moreover, effects of climate change vary from region to region. For example, extreme storm intensities are projected to increase in some areas of Europe even though summer precipitation is generally projected to decrease (Christensen and Christensen 2003; Kyselý et al.

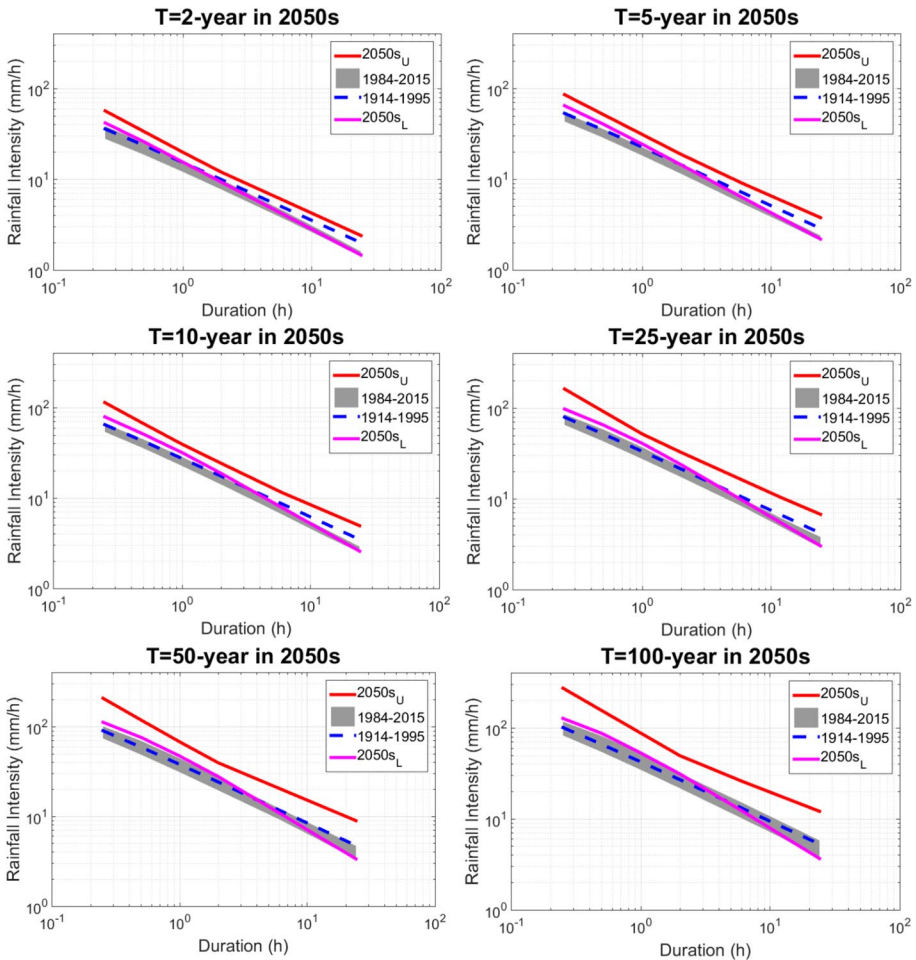


Fig. 4 Comparisons of past (1914–1995) IDF curves (blue dash line), current (1984–2015) IDF curves (gray shaded area), and WRF projected (red and magenta lines) IDF curves of the 2050s. Red and magenta lines stand for upper and lower bounds of projected IDF curves, respectively, which are estimated from RCP 4.5 and RCP 8.5 scenarios of all four GCMs downscaled together

2012). In contrast, mixed changes in rainfall had been observed over Africa in 1983–2010: increase in annual Sahel rainfall (over 30 mm yr⁻¹ per decade), decrease in March–May East African rainfall (–65 mm yr⁻¹ per decade), increase in annual Southern Africa rainfall (35 mm yr⁻¹ per decade), varying changes in Central Africa annual rainfall (Maidment et al. 2015), and more severe droughts in sub-Sahara of Africa (Gizaw and Gan 2016).

4.2 Comparisons between past (1914–1995), reference (1984–2015), and future (2041–2100) IDF curves

First, we investigated variations between the past (1914–1995) and the reference (1984–2015) IDF curves of Edmonton. Rain gauge data at the Edmonton Municipal

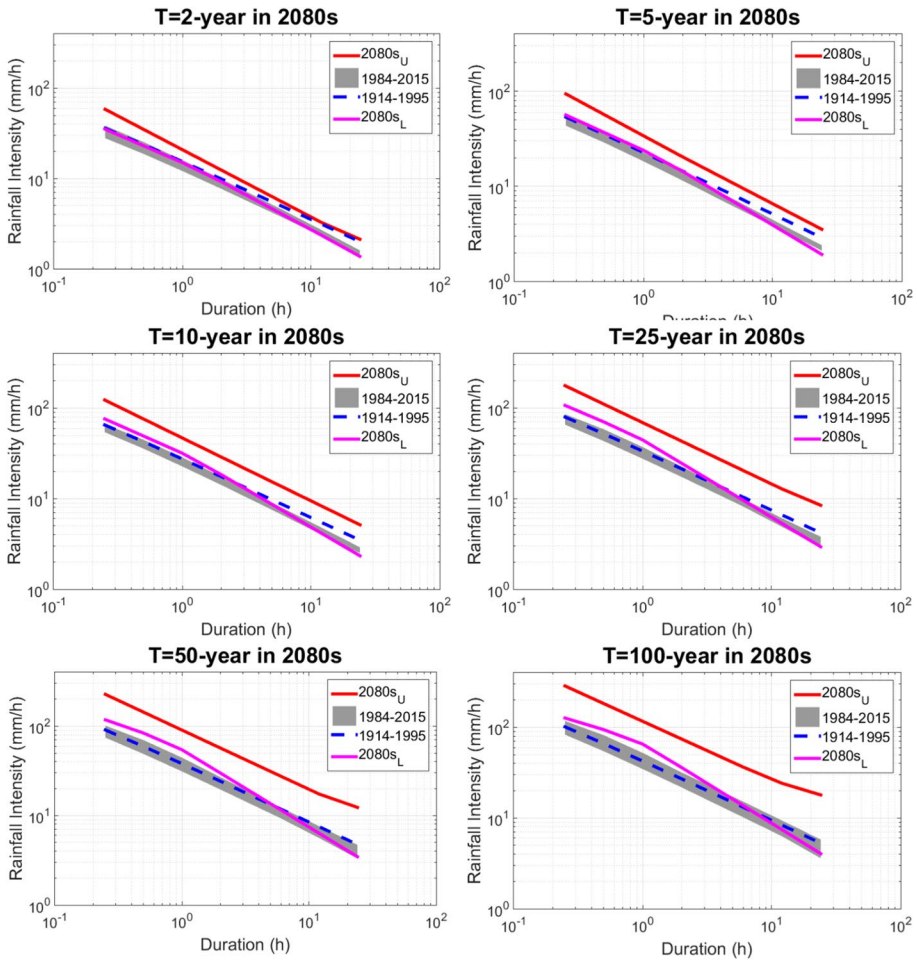


Fig. 5 Comparisons of past (1914–1995) IDF curves (blue dash line), current (1984–2015) IDF curves (gray shaded area), and WRF projected (red and magenta lines) IDF curves of the 2080s. Red and magenta lines stand for upper and lower bounds of projected IDF curves, respectively, which are estimated from RCP 4.5 and RCP 8.5 scenarios of all four GCMs downscaled together

Airport were applied to derive the past IDF curves. The rainfall records at 11 rain gauges (Fig. 2) were used to develop the reference IDF curves. The upper and lower bounds of IDF curves were estimated based on IDF curves at 11 sites (shaded gray zones in Figs. 4 and 5). For return periods smaller than 25 years, intensities of past IDF curves are higher than intensities of the reference (1984–2015) IDF curves of Edmonton but for storm durations > 4 h. For the 50-year return period, intensities based on the upper bound of the reference IDF curves are higher than past IDF curves. For ≤ 4-h storms, intensities for the lower bounds of reference IDF curves are marginally higher than that of past IDF curves especially for 2080s. Our results are similar with other studies, such as Lenderink and Van Meijgaard (2008) and O’Gorman (2015) who found that intensities of storms of short durations tend to be more sensitive to temperature change. Based on upper bounds of the reference IDF estimates, extreme storms of all durations are more sensitive to higher temperature,

but not so based on the lower bounds of the reference IDF estimates especially for long-duration storms. For return periods larger than 100 years, intensities of the upper bound of reference IDF curves are predominantly larger than intensities of past IDF curves for all durations of storms.

By comparing the past and the reference IDF curves, it seems that storms of short durations (≤ 4 h) in Edmonton dominated by convective storms in MJJA may or may not be more extreme than storms of long durations. On the other hand, the intensity of long-duration storms (> 4 h in Edmonton) of the reference IDF curves has been lower than the past probably because only limited extreme stratiform storms have been observed in 1984–2015. The uncertainty associated with IDF curves could be related to multi-decade climate oscillations, different climate baseline periods, or different GEV distribution parameters estimation methods (Willems 2013; Fadhel et al. 2017). The reference IDF curves developed out of the 1984–2015 rain gauge data of Edmonton are consistent with extreme storms that flooded Edmonton in July 2004, 2009, and 2012, respectively.

Next, the reference (1984–2015) IDF curves are compared with that projected for the 2050s (2041–2070) and 2080s (2071–2100) (Figs. 4 and 5), respectively. Intensive storms are projected to occur in the future, especially for storms of short durations (≤ 1 h). The projected lower bound of IDF curves in 2050s (solid lines) has higher intensities than those of the reference (1984–2015) IDF curves (shaded gray) for short-duration storms (Figs. 4 and 5). The projected upper bound of IDF curves in the 2050s have higher intensities than the reference (1984–2015) IDF curves (shaded gray) for storms of all durations and of all return periods. For durations of storms larger than 1 h, the lower bound of projected IDF curves of the 2050s overlaps with that of the reference IDF curves. However, overlapped areas between the projected and the reference IDF curves for storms of longer durations are small compared to non-overlapped areas. Overall, the highest projected increase in intensities is generally storms of about 15-min durations, with a maximum increase of 143%, a median increase of 47.9%, and a minimum change of -8.7% among all return periods. For storms of 25-year return period, the maximum and median projected changes are all positive for storms of all durations. Projected minimum and median changes tend to increase with a decrease in storm durations. The projected maximum change is marginally lower for storms of 1- to 2-h durations. More details on changes of future rainfall intensities are shown in Table 1, Tables S1.1–S1.6, and Tables S2.1–S2.6. The minimum, median, and maximum percentage changes were derived from eight sets of RCP projections. As expected, projected IDF curves for the 2080s (Figs. 4 and 5) generally exhibit higher intensities than those of the 2050s (Table 1). Overall, storm intensities of central Alberta are projected to increase from the 2050s to 2080s for storms of short durations and return periods of larger than 25 years.

4.3 Comparisons between future (2041–2100) IDF curves projected using WRF and RCP climate scenarios with those using MM5 and SRES climate scenarios

Kuo et al. (2015) set up a RCM called MM5 of NCAR in a one-way (stand-alone), three-domain nested framework to simulate future MJJA precipitation of central Alberta. MM5 was forced with climate data of four GCMs, CGCM3 (Canadian GCM), ECHAM5 (German GCM), CCSM3 (Community Climate Systems Model of USA), and MIROC3.2 (Japanese GCM, Model for Interdisciplinary Research on Climate) for 2011–2100 based on the SRES A2, A1B, and B1 of Assessment Report #4 of IPCC (2007).

Table 1 The maximum, median, and minimum changes (percentage) in the 2050s and 2080s with respect to 1984–2015, for return periods ranging from 2 to 100 years

Stage	Duration (h)	T = 2 years			T = 5 years			T = 10 years		
		Min	Med	Max	Min	Med	Max	Min	Med	Max
2050s	0.25	8.7	21.8	47.6	20.4	39.1	59.3	19.3	45.7	71.8
	0.5	2.6	15.0	33.1	13.3	24.4	44.9	14.2	26.5	49.4
	1	-3.0	9.5	24.4	7.6	17.8	37.8	11.5	18.0	38.2
	2	-6.3	5.9	20.8	3.2	14.2	34.7	7.3	16.6	38.7
	6	-8.8	7.1	30.7	-1.9	14.2	40.7	-0.8	17.5	45.6
	12	-9.1	9.2	39.2	-4.8	14.4	49.7	-6.2	15.6	57.1
2080s	0.25	-8.3	9.8	50.1	-8.5	13.4	57.7	-10.9	12.3	70.5
	0.5	-8.7	27.9	51.7	4.2	46.0	73.9	14.0	59.2	84.2
	1	-9.1	16.6	38.1	2.4	30.8	57.8	9.7	36.3	69.4
	2	-6.1	10.3	30.3	5.3	22.8	49.7	11.1	27.8	63.8
	6	-6.6	3.4	25.6	2.8	14.6	46.0	5.0	18.5	64.4
	12	-11.1	3.9	21.8	-7.7	15.9	46.8	-6.2	21.6	70.6
2050s	0.25	-12.6	4.3	21.1	-13.6	18.5	47.7	-13.3	23.2	73.4
	0.5	-14.3	6.9	32.8	-20.0	19.3	47.1	-19.4	26.0	77.3
	1	-14.3	6.9	32.8	-20.0	19.3	47.1	-19.4	26.0	77.3
	2	-14.3	6.9	32.8	-20.0	19.3	47.1	-19.4	26.0	77.3
	6	-14.3	6.9	32.8	-20.0	19.3	47.1	-19.4	26.0	77.3
	12	-14.3	6.9	32.8	-20.0	19.3	47.1	-19.4	26.0	77.3
2080s	0.25	-14.3	6.9	32.8	-20.0	19.3	47.1	-19.4	26.0	77.3
	0.5	-14.3	6.9	32.8	-20.0	19.3	47.1	-19.4	26.0	77.3
	1	-14.3	6.9	32.8	-20.0	19.3	47.1	-19.4	26.0	77.3
	2	-14.3	6.9	32.8	-20.0	19.3	47.1	-19.4	26.0	77.3
	6	-14.3	6.9	32.8	-20.0	19.3	47.1	-19.4	26.0	77.3
	12	-14.3	6.9	32.8	-20.0	19.3	47.1	-19.4	26.0	77.3

Table 1 (continued)

2080s	0.25	24.9	72.6	106.2	16.2	77.8	123.8	7.7	84.6	143.1
	0.5	20.5	41.9	89.4	19.9	44.5	105.4	15.1	47.4	123.1
	1	19.7	31.4	85.8	22.4	31.7	103.2	24.8	36.4	122.5
	2	8.5	26.2	90.3	11.1	32.3	111.4	13.3	38.0	133.4
	6	-3.7	28.4	105.2	-6.1	27.2	123.9	-9.7	24.1	140.4
	12	-12.7	27.4	110.2	-16.8	22.9	128.9	-20.7	20.6	157.4
	24	-22.5	24.2	122.6	-26.3	19.8	162.6	-30.2	17.6	210.0

As a newer regional climate model of NCAR, WRF has more and better parameterization schemes than MM5. From various test runs, the schemes of WRF chosen are the Kain-Fritsch cumulus parameterization scheme, WRF Double-Moment 6-class Microphysics scheme, shortwave (Dudhia, CAM, and RRTMG) and longwave radiation scheme (RRTM, CAM, and RRTMG), and the Yonsei University PBL scheme. Unlike MM5, WRF is also coupled to the Noah land surface scheme to account for the land–atmosphere interaction and feedback to enhance the predictability of WRF in simulating convective storms, and to reduce simulation errors in heat and water fluxes, which could affect humidity, temperature, and precipitation. The baseline regional climate of central Alberta simulated by WRF in a coupled mode (2-way) agrees well with gridded observed climate data of Environment Canada. After bias correction, precipitation generated by MM5 is less accurate than that simulated by the WRF-Noah coupled system, which is expected. An examination of the moisture advection for individual over-simulation cases suggests that MM5 may not properly handle the redistribution of moisture in regions of complex terrain (Gilliam and Pleim 2010; Hanna et al. 2010; Steeneveld et al. 2010).

Even though future IDF curves for central Alberta were also projected upward, the average storm intensity is projected to increase by about 29% by the 2080s. As a whole, the projected changes of IDF curves of Kuo et al. (2015) are relatively modest compared to the projected changes of IDF curves derived from simulations of WRF driven by RCP climate scenarios for central Alberta in 2050s and 2080s, particularly for projected maximum changes (%) (Fig. 6).

Firstly, SRES climate scenarios of IPCC (2007) relied on research processes based on limited exchanges of information among physical, biological, and social scientists (Moss et al. 2010). The implications of climate change depend not only on the Earth system’s responses to changes in radiative forcing, but also on how human society responds to changes in economies, technology, fossil fuel consumption, lifestyle, and policy. In contrast, Representative Concentration Pathways (RCP) of IPCC (2013) were developed from a newer process toward the goal of integrating socioeconomic development and scientific advances such as improved representation of the terrestrial carbon cycle in climate and integrated assessment models. RCP climate scenarios are developed from identifying radiative forcing characteristics that support modeling a wide range of plausible future climates in response to possible changes in economies,

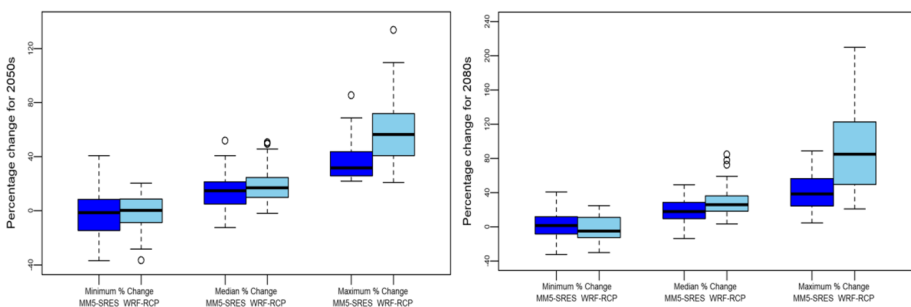


Fig. 6 Comparison of boxplots of projected maximum, median, and minimum changes (percentage) by MM5 forced with SRES climate scenarios and by WRF forced with RCP climate scenarios, in the 2050s and 2080s with respect to 1984–2015, for return periods ranging from 2 to 100 years, respectively

technology, fossil fuel consumption, lifestyle, and policy (Moss et al. 2010). RCPs were selected to provide needed inputs of emissions, concentrations, and land use/cover for climate models.

Second, SRES, A2, A1B, and B1 of four GCMs of IPCC (2007) for central Alberta were downscaled using an “older” RCM called MM5, which is the fifth-generation, mesoscale atmospheric model of National Center for Atmospheric Research, NCAR/Penn State University (Hanrahan et al. 2015). In contrast, WRF is the latest, non-hydrostatic atmospheric model originally based on the MM5 model. MM5 is no longer been updated, while WRF has been widely used besides research purposes (Wilmot et al. 2014). Several studies have compared the performance between WRF and MM5 (Gilliam and Pleim 2010; Awan et al. 2011; Gsella et al. 2014; Wilmot et al. 2014). The choice of physical parameterization is sensitive in both models, but WRF is more sensitive than MM5 (Awan et al. 2011). Gsella et al. (2014) found that the performance of both models is similar, but WRF is better in reproducing the annual average of precipitation and relative humidity. However, simulating extreme rainfall is a challenge to both RCMs. In general, the consensus is that WRF outperforms MM5 (Gilliam and Pleim 2010; Hanna et al. 2010; Steeneveld et al. 2010). Moreover, WRF is coupled to a land surface scheme to account for land–atmosphere feedback, while Kuo et al. (2015) set up MM5 in a stand-alone mode. Albeit it is unknown how the climate will evolve over the twenty-first century under the impacts of global warming and other environmental changes, results of this study should be more representative than that of Kuo et al. (2015).

4.4 Recommendations for future works

There are other approaches available to construct future IDF curves. For example, the IDF_CC Tool (Simonovic et al. 2016; Schardong et al. 2020) uses various statistical downscaling approaches to project future IDF curves. Statistical downscaling approaches are viable alternatives given climate change scenarios of more GCMs can be considered in projecting future IDF curves as statistical downscaling methods require much less computations compared to dynamic downscaling methods using regional climate models such as WRF. However, the validity of empirical relationships developed for the baseline period applied to project future extreme events simulated by GCMs is unknown (unclear). Therefore, comparisons between different downscaling methods are recommended for further studies. In addition, flood risk assessments and flood mitigation plans should also be conducted for regions vulnerable to flooding.

Bias correction methods such as the quantile–quantile bias correction used in this study, which assumes a stationary empirical relationship between modeled and observed rainfall, have drawbacks because this assumption can be violated. There have been works published specifically to address such issues, e.g., Ehret et al. (2012), Bock et al. (2018), and (Lanzante et al. 2018). Furthermore, atmospheric dynamics in extreme rainfall (Palmer 2013), storm track shifts (Shaw et al. 2016), and others could affect projected extreme events. The limitations of dynamically downscaling RCP climate scenarios of GCMs by a RCM and biased corrected by a bias correction scheme should be further investigated, including applying more RCMs to dynamically downscaled climate scenarios of GCMs, to evaluate uncertainties related to RCMs selected for projecting climate change impacts on changes of future IDF curves.

5 Summary and conclusions

Based on the results obtained from two RCP climate scenarios, RCP 4.5 and RCP 8.5 dynamically downscaled by the RCM, WRF, both air temperature and CAPE in central Alberta are projected to increase in the 2050s. However, for the 2080s, WRF projected a larger increase in air temperature and CAPE under RCP 8.5, while under RCP 4.5 scenarios, it projected a relatively modest increase. The air temperature is projected to increase from 0.019 to 0.088 °C/year in 2041–2100. With reference to the baseline of 1980–2005, air temperature of central Alberta is projected to increase by about an average of 4.6–6.3 °C in the 2080s under RCP 8.5 scenario. Compared to air temperature, CAPE is projected to increase at modest, non-significant rates annually under RCP 4.5 scenarios, but it is projected to increase under RCP 8.5 scenarios at rates ranging from 0.2 to 1.4%/year in 2041–2100, with an average projected increase of about 56–119% in 2041–2100.

A quantile–quantile bias correction method was applied to correct the bias of extreme storms over-simulated by WRF for both the base period, the 2050s and 2080s, assuming that the empirical relationship between simulated and observed rainfall intensities will not change for future storms of higher intensities under the RCP climate scenarios considered in this study. According to projected IDF curves developed from WRF's simulations, it seems that future storms of central Alberta will become more intensive, especially for short-duration storms (≤ 1 h). In one extreme case, the projected intensity for short-duration storms (≤ 1 h) could increase up to 143% in the 2080s. Moreover, for storms of low return periods (2 years and 5 years), the projected intensities are generally higher in all durations of storms considered, with the projected change ranging from –20 to 74% in the 2080s.

Return periods of short- to moderate-duration storms (≤ 4 h) are projected to decrease significantly in 2041–2100 in both upper and lower bounds of projected IDF curves, which implies much higher risk of flooding in the future. On the other hand, based on differences between the upper (lower) bound of the baseline intensity and that of the future intensity, return periods of long-duration storms, e.g., 24 h, tend to decrease (increase). From the projected increase in intensities of short-duration storms, it means that central Alberta could suffer from more frequent and severe flooding due to the occurrence of more intensive storms of short durations in the future.

Supplementary Information The online version contains supplementary material available at <https://doi.org/10.1007/s10584-021-03250-6>.

Acknowledgements We are grateful to Compute Canada's WestGrid for its assistance with technical issues of its supercomputers. This research was supported by the Natural Sciences and Engineering Research Council (NSERC) of Canada.

Author contribution T. Y. Gan conceived the research ideas, C. C. Kuo conducted the experiments, and C. C. Kuo, K. E. Gan, Y. Yang, and T. Y. Gan wrote and revised the manuscript.

Funding The research is partly funded by the Natural Science and Engineering Research Council of Canada and the City of Edmonton.

Availability of data and materials The data and materials are available from the corresponding author upon reasonable request.

Declarations

Ethics approval No ethical approval is necessary as the research does not involve human or animals.

Consent to participate All authors consent to participate in the research.

Consent to publish All authors consent to publish the research findings.

Competing interests The authors declare no competing interests.

References

- Adler RF, Gu G, Sapiano M, Wang J-J, Huffman GJ (2017) Global precipitation: Means, variations and trends during the satellite era (1979–2014). *Surv Geophys* 38(4):679–699. <https://doi.org/10.1007/s10712-017-9416-4>
- Alexander LV et al (2006) Global observed changes in daily climate extremes of temperature and precipitation. *J Geophys Res* 111(D5):D05109. <https://doi.org/10.1029/2005JD006290>
- Allan RP, Soden BJ (2008) Atmospheric Warming and the Amplification of Precipitation Extremes. *Science*. American Association for the Advancement of Science 321(5895):1481–1484. <https://doi.org/10.1126/science.1160787>
- Awan NK, Truhetz H, Gobiet A (2011) Parameterization-induced error characteristics of MM5 and WRF operated in climate mode over the alpine region: An ensemble-based analysis. *J Clim* 24(12):3107–3123. <https://doi.org/10.1175/2011JCLI3674.1>
- Berg P, Moseley C, Haerter JO (2013) Strong increase in convective precipitation in response to higher temperatures. *Nat Geosci* 6(3):181–185. <https://doi.org/10.1038/ngeo1731>
- Bintanja R, Selten FM (2014) Future increases in Arctic precipitation linked to local evaporation and sea-ice retreat. *Nature* 509(7501):479–482. <https://doi.org/10.1038/nature13259>
- Bock AR, Hay LE, McCabe GJ, Markstrom SL, Dwight AR (2018) Do downscaled general circulation models reliably simulate historical climatic conditions? *Earth Interact* 22(10):1–22. <https://doi.org/10.1175/EI-D-17-0018.1>
- Boé J, Terray L, Habets F, Martin E (2007) Statistical and dynamical downscaling of the Seine basin climate for hydro-meteorological studies. *Int J Climatol* 27(12):1643–1655. <https://doi.org/10.1002/joc.1602>
- Chen F, Janjić Z, Mitchell K (1997) Impact of atmospheric surface-layer parameterizations in the new land-surface scheme of the NCEP mesoscale Eta model. *Bound-Layer Meteorol*. Springer Netherlands 85(3):391–421. <https://doi.org/10.1023/A:1000531001463>
- Chen F, Mitchell K, Schaake J, Xue Y, Pan HL, Koren V, Duan QY, Ek M, Betts A (1996) Modeling of land surface evaporation by four schemes and comparison with FIFE observations. *J Geophys Res Atmos*. Blackwell Publishing Ltd 101(D3):7251–7268. <https://doi.org/10.1029/95JD02165>
- Chou C, Chen CA, Tan PH, Chen KT (2012) Mechanisms for global warming impacts on precipitation frequency and intensity. *J Clim* 25(9):3291–3306. <https://doi.org/10.1175/JCLI-D-11-00239.1>
- Christensen JH, Christensen OB (2003) Severe summertime flooding in Europe. *Nature*. Nature Publishing Group 421(6925):805–806. <https://doi.org/10.1038/421805a>
- Collins WD, Rasch PJ, Boville BA, Hack JJ, McCaa JR, Williamson DL, Kiehl JT, Briegleb B (2004) Description of the NCAR Community Atmosphere Model (CAM3.0). Boulder, CO
- Dong W, Lin Y, Wright JS, Xie Y, Yin X, Guo J (2018) Precipitable water and CAPE dependence of rainfall intensities in China. *Clim Dyn*. Springer Berlin Heidelberg:1–12. <https://doi.org/10.1007/s00382-018-4327-8>
- Douville H, Raghavan K, Renwick J, Allan RP, Arias PA, Barlow M, Cerezo-Mota R, Cherchi A, Gan TY et al (2021) Water Cycle Changes. In: Masson-Delmotte VP et al (eds) *Climate Change 2021: The Physical Science Basis*. Contribution of Working Group I to the Sixth Assessment Report of the Intergovernmental Panel on Climate Change. Cambridge University Press
- Ehret U, Zehe E, Wulfmeyer V, Warrach-Sagi K, Liebert J (2012) HESS Opinions “should we apply bias correction to global and regional climate model data?” *Hydrol Earth Syst Sci* 16(9):3391–3404. <https://doi.org/10.5194/hess-16-3391-2012>
- ECCC (Environment and Climate Change Canada) (2017) Top ten weather stories for 2004
- Erfani A et al (2003) Synoptic and mesoscale study of a severe convective outbreak with the nonhydrostatic Global Environmental Multiscale (GEM) model. *Meteorol Atmos Phys* 82(1–4):31–53. <https://doi.org/10.1007/s00703-001-0585-8>
- Fadhel S, Rico-Ramirez MA, Han D (2017) Uncertainty of Intensity–Duration–Frequency (IDF) curves due to varied climate baseline periods. *J Hydrol* 547:600–612. <https://doi.org/10.1016/j.jhydrol.2017.02.013>

- Flato G et al (2013) Evaluation of Climate Models. In: Stocker TF et al (eds) Climate Change 2013: The Physical Science Basis. Contribution of WG I to the 5th Assessment Report of the Intergovernmental Panel on Climate Change. Cambridge University Press, Cambridge and New York
- Frich P, Alexander LV, Della-Marta P, Gleason B, Haylock M, Tank Klein AMG, Peterson T (2002) Observed coherent changes in climatic extremes during the second half of the twentieth century. *Clim Res* 19(3):193–212. <https://doi.org/10.3354/cr019193>
- Gilliam RC, Pleim JE (2010) Performance assessment of new land surface and planetary boundary layer physics in the WRF-ARW. *J Appl Meteorol Climatol. American Meteorological Society* 49(4):760–774. <https://doi.org/10.1175/2009JAMC2126.1>
- Gizaw M, Gan KE, Yang Y, T. Y., Gan, (2021) Trends in Convective Available Potential Energy (CAPE) and extreme precipitation indices over the United States and southern Canada for summer of 1979–2013. *J Phys Chem Earth. Elsevier Sc.*<https://doi.org/10.1016/j.pce.2021.103047>
- Gizaw MS, Gan TY (2016) Impact of climate change and El Niño episodes on droughts in sub-Saharan Africa. *Clim Dyn.* <https://doi.org/10.1007/s00382-016-3366-2>
- Gsella A, De Meij A, Kerschbaumer A, Reimer E, Thunis P, Cuvelier C (2014) Evaluation of MM5, WRF and TRAMPER meteorology over the complex terrain of the Po Valley, Italy. *Atmos Environ* 89:797–806. <https://doi.org/10.1016/j.atmosenv.2014.03.019>
- Hanna SR et al (2010) Comparison of observed, MM5 and WRF-NMM model-simulated, and HPAC-assumed boundary-layer meteorological variables for 3 days during the IHOP field experiment. *Bound-Layer Meteorol. Springer* 134(2):285–306. <https://doi.org/10.1007/s10546-009-9446-7>
- Hanrahan J, Kuo C-C, Gan TY (2015) Configuration and validation of a mesoscale atmospheric model for simulating summertime rainfall in Central Alberta. *Int J Climatol. John Wiley and Sons Ltd* 35(5):660–675. <https://doi.org/10.1002/joc.4011>
- Hassanzadeh E, Nazemi A, Elshorbagy A (2014) Quantile-based downscaling of precipitation using genetic programming: Application to IDF curves in Saskatoon. *J Hydrol Eng. American Society of Civil Engineers (ASCE)* 19(5):943–955. [https://doi.org/10.1061/\(ASCE\)HE.1943-5584.0000854](https://doi.org/10.1061/(ASCE)HE.1943-5584.0000854)
- Hong SY, Noh Y, Dudhia J (2006) A new vertical diffusion package with an explicit treatment of entrainment processes. *Mon Weather Rev* 134(9):2318–2341. <https://doi.org/10.1175/MWR3199.1>
- Hosking JRM, Wallis JR (1997) *Regional Frequency Analysis: An Approach Based on L-Moments.* Cambridge University Press
- IPCC (2007) *IPCC Fourth Assessment Report: Working Group I (WGI) report*
- IPCC (2013) *IPCC Fourth Assessment Report: Working Group I (WGI) report*
- Jenkinson AF (1955) The Frequency Distribution of the Annual Maximum (or Minimum) Values of Meteorological Elements. *Q J R Meteorol Soc* 87:158
- Jiang R, Gan TY, Xie J, Wang N, Kuo CC (2015) Historical and potential changes of precipitation and temperature of Alberta subjected to climate change impact: 1900–2100. *Theor Appl Climatol. Springer Vienna* 127(3–4):725–739. <https://doi.org/10.1007/s00704-015-1664-y>
- Johnson F, Sharma A (2011) Accounting for interannual variability: A comparison of options for water resources climate change impact assessments. *Water Resour Res* 47(4). <https://doi.org/10.1029/2010WR009272>
- Kain JS (2004) The Kain-Fritsch Convective Parameterization: An Update. *J Appl Meteorol* 43(1):170–181. [https://doi.org/10.1175/1520-0450\(2004\)043%3c0170:TKCPAU%3e2.0.CO;2](https://doi.org/10.1175/1520-0450(2004)043%3c0170:TKCPAU%3e2.0.CO;2)
- Kanamitsu M, Mo KC (2003) Dynamical effect of land surface processes on summer precipitation over the Southwestern United States. *J Clim* 16(3):496–509. [https://doi.org/10.1175/1520-0442\(2003\)016%3c0496:DEOLSP%3e2.0.CO;2](https://doi.org/10.1175/1520-0442(2003)016%3c0496:DEOLSP%3e2.0.CO;2)
- Kendall MG (1948) *Rank correlation methods.* Griffin, London
- Kerkhoven E, Gan TY, Shiiba M, Reuter G, Tanaka K (2006) A comparison of cumulus parameterization schemes in a numerical weather prediction model for a monsoon rainfall event. *Hydrol Process. John Wiley & Sons, Ltd* 20(9):1961–1978. <https://doi.org/10.1002/hyp.5967>
- Kuo C-C, Gan TY (2015) Risk of Exceeding Extreme Design Storm Events under Possible Impact of Climate Change. *J Hydrol Eng* 20(12):04015038. [https://doi.org/10.1061/\(asce\)jhe.1943-5584.0001228](https://doi.org/10.1061/(asce)jhe.1943-5584.0001228)
- Kuo C-C, Gan TY (2018) Estimation of precipitation and air temperature over western Canada using a regional climate model. *Int J Climatol. Wiley-Blackwell.* <https://doi.org/10.1002/joc.5716>
- Kuo C-C, Gan TY, Gizaw M (2015) Potential impact of climate change on intensity duration frequency curves of central Alberta. *Clim Change* 130(2):115–129. <https://doi.org/10.1007/s10584-015-1347-9>
- Kuo CC, Gan TY, Chan S (2013) Regional intensity-duration-frequency curves derived from ensemble empirical mode decomposition and scaling property. *J Hydrol Eng* 18(1):66–74. [https://doi.org/10.1061/\(ASCE\)HE.1943-5584.0000612](https://doi.org/10.1061/(ASCE)HE.1943-5584.0000612)

- Kuo CC, Gan TY, Hanrahan JL (2014) Precipitation frequency analysis based on regional climate simulations in Central Alberta. *J. Hydrol. Elsevier B.V.* 510:436–446. <https://doi.org/10.1016/j.jhydrol.2013.12.051>
- Kyselý J et al (2012) Different patterns of climate change scenarios for short-term and multi-day precipitation extremes in the Mediterranean. *Glob Planet Chang* 98–99:63–72. <https://doi.org/10.1016/j.gloplacha.2012.06.010>
- Lafon T, Dadson S, Buys G, Prudhomme C (2013) Bias correction of daily precipitation simulated by a regional climate model: A comparison of methods. *Int J Climatol* 33(6):1367–1381. <https://doi.org/10.1002/joc.3518>
- Lanzante JR et al (2018) Some pitfalls in statistical downscaling of future climate. *Bull Am Meteor Soc* 99(4):791–803. <https://doi.org/10.1175/BAMS-D-17-0046.1>
- Lenderink G, Van Meijgaard E (2008) Increase in hourly precipitation extremes beyond expectations from temperature changes. *Nat Geosci. Nature Publishing Group* 1(8):511–514. <https://doi.org/10.1038/ngeo262>
- Lim KSS, Hong SY (2010) Development of an effective double-moment cloud microphysics scheme with prognostic cloud condensation nuclei (CCN) for weather and climate models. *Mon Weather Rev. American Meteorological Society* 138(5):1587–1612. <https://doi.org/10.1175/2009MWR2968.1>
- Mahmood R, Littell A, Hubbard KG, You J (2012) Observed data-based assessment of relationships among soil moisture at various depths, precipitation, and temperature. *Appl Geogr. Elsevier BV* 34:255–264. <https://doi.org/10.1016/j.apgeog.2011.11.009>
- Maidment RL, Allan RP, Black E (2015) Recent observed and simulated changes in precipitation over Africa. *Geophys Res Lett* 42(19):8155–8164. <https://doi.org/10.1002/2015GL065765>
- Mailhot A et al (2012) Future changes in intense precipitation over Canada assessed from multi-model NARC-CAP ensemble simulations. *Int J Climatol* 32(8):1151–1163. <https://doi.org/10.1002/joc.2343>
- Mailhot A, Kingumbi A, Talbot G, Poulin A (2010) Future changes in intensity and seasonal pattern of occurrence of daily and multi-day annual maximum precipitation over Canada. *J Hydrol. Elsevier* 388(3–4):173–185. <https://doi.org/10.1016/j.jhydrol.2010.04.038>
- Mann HB (1945) Nonparametric tests against trend. *Econometrica* 13(3):245–259
- Maurer EP, Brekke L, Pruitt T, Duffy PB (2007) Fine-resolution climate projections enhance regional climate change impact studies. *EOS Trans Am Geophys. Union American Geophysical Union (AGU)* 88(47):504–504. <https://doi.org/10.1029/2007eo470006>
- Milrad SM, Gyakum JR, Atallah EH (2015) A Meteorological Analysis of the 2013 Alberta Flood: Antecedent Large-Scale Flow Pattern and Synoptic-Dynamic Characteristics. *Mon Weather Rev* 143(7):2817–2841. <https://doi.org/10.1175/MWR-D-14-00236.1>
- Mladjic B, Sushama L, Khaliq MN, Laprise R, Caya D, Roy R (2011) Canadian RCM Projected Changes to Extreme Precipitation Characteristics over Canada. *J Clim* 24(10):2565–2584. <https://doi.org/10.1175/2010JCLI3937.1>
- Moss RH, Edmonds JA, Hibbard KA, Manning MR, Rose SK, Van Vuuren DP, Carter TR, Emori S, Kainuma M et al (2010) The next generation of scenarios for climate change research and assessment. *Nature. Nature Publishing Group* 463(7282):747–756. <https://doi.org/10.1038/nature08823>
- Murugavel P, Pawar SD, Gopalakrishnan V (2012) Trends of Convective Available Potential Energy over the Indian region and its effect on rainfall. *Int J Climatol. John Wiley & Sons, Ltd.* 32(9):1362–1372. <https://doi.org/10.1002/joc.2359>
- O’Gorman PA (2015) Precipitation extremes under climate change. *Curr Clim Change Rep* 1(2):49–59. <https://doi.org/10.1007/s40641-015-0009-3>
- Palmer TN (2013) Climate extremes and the role of dynamics. *Proc Natl Acad Sci* 110(14):5281–5282. <https://doi.org/10.1073/pnas.1303295110>
- Pendergrass AG, Hartmann DL (2014) Changes in the distribution of rain frequency and intensity in response to global warming. *J Clim* 27(22):8372–8383. <https://doi.org/10.1175/JCLI-D-14-00183.1>
- Pendergrass AG, Knutti R, Lehner F, Deser C, Sanderson BM (2017) Precipitation variability increases in a warmer climate. *Sci Rep. Nature Publishing Group* 7(1):1–9. <https://doi.org/10.1038/s41598-017-17966-y>
- Ryu YH, Smith JA, Bou-Zeid E, Baeck ML (2016) The influence of land surface heterogeneities on heavy convective rainfall in the baltimore-washington metropolitan area. *Mon Weather Rev*:553–573
- Schardong A, Simonovic SP, Gaur A, Sandink D (2020) Web-based tool for the development of intensity duration frequency curves under changing climate at gauged and ungauged locations. *Water* 12(5). <https://doi.org/10.3390/W12051243>
- Scheepers H, Wang J, Gan TY, Kuo CC (2018) The impact of climate change on inland waterway transport: effects of low water levels on the Mackenzie River. *J Hydrol. Elsevier.* <https://doi.org/10.1016/J.JHYDR.OL.2018.08.059>
- Seeley JT, Romps DM (2015) Why does tropical convective available potential energy (CAPE) increase with warming? *Geophys Res Lett* 42(23):10429–10437. <https://doi.org/10.1002/2015GL066199>
- Sen PK (1968) Estimates of the Regression Coefficient Based on Kendall’s Tau. *J Am Stat Assoc* 63(324):1379–1389. <https://doi.org/10.2307/2285891>

- Shaw TA et al (2016) Storm track processes and the opposing influences of climate change. *Nat Geosci* 9(9):656–664. <https://doi.org/10.1038/ngeo2783>
- Shepherd A, McGinn SM (2003) Assessment of climate change on the Canadian Prairies from downscaled GCM data. *Atmosphere-Ocean* 41(4):301–316. <https://doi.org/10.3137/ao.410404>
- Shi X, Xu X (2008) Interdecadal trend turning of global terrestrial temperature and precipitation during 1951–2002. *Prog Nat Sci. Science Press* 18(11):1383–1393. <https://doi.org/10.1016/j.pnsc.2008.06.002>
- Sillmann J, Kharin VV, Zwiers FW, Zhang X, Bronaugh D (2013) Climate extremes indices in the CMIP5 multimodel ensemble: Part 2. Future climate projections. *J Geophys Res Atmos. Wiley-Blackwell* 118(6):2473–2493. <https://doi.org/10.1002/jgrd.50188>
- Simonovic SP, Schardong A, Sandink D, Srivastav R (2016) A web-based tool for the development of Intensity Duration Frequency curves under changing climate. *Environ Model Softw* 81:136–153. <https://doi.org/10.1016/j.envsoft.2016.03.016>
- Skamarock WC, Klemp JB, Dudhia J, Gill DO, Barker DM, Duda MG, Huang X-Y, Wang W, Powers JG (2008) A description of the advanced research WRF version 3. NCAR Technical Note. Boulder, CO
- Steenefeld GJ, Wokke MJJ, Groot Zwaafink CD, Pijlman S, Heusinkveld BG, Jacobs AFG, Holtslag AAM (2010) Observations of the radiation divergence in the surface layer and its implication for its parameterization in numerical weather prediction models. *J Geophys Res Atmos. Blackwell Publishing Ltd* 115(6). <https://doi.org/10.1029/2009JD013074>
- Sun F, Roderick ML, Lim WH, Farquhar GD (2011) Hydroclimatic projections for the Murray-Darling Basin based on an ensemble derived from Intergovernmental Panel on Climate Change AR4 climate models. *Water Resour Res* 47(4). <https://doi.org/10.1029/2010WR009829>
- Tariku TB, Gan TY (2018) Regional climate change impact on extreme precipitation and temperature of the Nile river basin. *Clim Dyn. Springer* 0(0):1–20. <https://doi.org/10.1007/s00382-018-4092-8>
- Tariku TB, Gan TY (2018b) Sensitivity of the weather research and forecasting model to parameterization schemes for regional climate of Nile River Basin. *Clim Dyn. Springer Verlag* 50(11–12):4231–4247. <https://doi.org/10.1007/s00382-017-3870-z>
- Theil H (1992) A rank-invariant method of linear and polynomial regression analysis. Springer, Dordrecht, pp 345–381
- Wang B, Zhang M, Wei J, Wang S, Li S, Ma Q, Li X, Pan S (2013) Changes in extreme events of temperature and precipitation over Xinjiang, northwest China, during 1960–2009. *Quat Int* 298:141–151. <https://doi.org/10.1016/j.quaint.2012.09.010>
- Weisman ML, Skamarock WC, Klemp JB (1997) The resolution dependence of explicitly modeled convective systems. *Mon Weather Rev. American Meteorological Society* 125(4):527–548. [https://doi.org/10.1175/1520-0493\(1997\)125%3c0527:TRDOEM%3e2.0.CO;2](https://doi.org/10.1175/1520-0493(1997)125%3c0527:TRDOEM%3e2.0.CO;2)
- Willems P (2013) Revision of urban drainage design rules after assessment of climate change impacts on precipitation extremes at Uccle, Belgium. *J Hydrol* 496:166–177. <https://doi.org/10.1016/j.jhydrol.2013.05.037>
- Wilmot CSM, Rappenglück B, Li X, Cuchiaro G (2014) MM5 v3.6.1 and WRF v3.5.1 model comparison of standard and surface energy variables in the development of the planetary boundary layer. *Geosci Model Dev* 7(6):2693–2707. <https://doi.org/10.5194/gmd-7-2693-2014>
- Xu Y, Yang ZL (2012) A method to study the impact of climate change on variability of river flow: An example from the Guadalupe River in Texas. *Clim Change* 113(3–4):965–979. <https://doi.org/10.1007/s10584-011-0366-4>
- Yang Y, Gan TY, Tan X (2019) Spatiotemporal changes in precipitation extremes over Canada and their teleconnections to large-scale climate patterns. *J Hydrometeorol*:275–296. <https://doi.org/10.1175/jhm-d-18-0004.1>
- Ye B, Del Genio AD, Lo KKW (1998) CAPE variations in the current climate and in a climate change. *J Clim* 11(8):1997–2015. [https://doi.org/10.1175/1520-0442\(1998\)011%3c1997:CVITHCC%3e2.0.CO;2](https://doi.org/10.1175/1520-0442(1998)011%3c1997:CVITHCC%3e2.0.CO;2)
- Zhang J, Wang WC, Leung LR (2008) Contribution of land-atmosphere coupling to summer climate variability over the contiguous United States. *J Geophys Res Atmos* 113(22). <https://doi.org/10.1029/2008JD010136>

Publisher's note Springer Nature remains neutral with regard to jurisdictional claims in published maps and institutional affiliations.